



Investigation of a 3D camera

Sandrine van Frank

Master of Science Thesis
Supervisor: Dr. Bertrand Noharet (Acreo AB)
Supervisors: Pr. Jens Aage Tellefsen, Pr. Lars-Gunnar Andersson (KTH)
Examiner: Pr. Fredrik Laurell (KTH)

Report no: acr-049863

Investigation of a 3D camera

Sandrine van Frank

February 15, 2011

Abstract

The feasibility of a simple and low-cost 3D time-of-flight imaging system is experimentally investigated. Using a conventional CCD camera, a fast opto-electronic shutter and a modulated light, the distance of an object in a scene is measured. The measurements are computed using a homodyne approach. The key component of the system is the opto-electronic shutter, for which a modulator developed by Acreo AB is used, and special attention was brought to characterize its properties.

The principle has been successfully demonstrated. For a modulation frequency of 15 MHz and a modulator contrast of 3:1, the depth accuracy of the system is evaluated to 3.3 cm at worst and the repeatability of the measurements to 3.6 cm on a range of 2 m. Indications to improve the system's resolution are detailed for future work.

List of Figures

2.1	Time-of-flight principle with a pulsed light	6
2.2	Time-of-flight principle with an AM light	7
3.1	Basic design of a 3D time-of-flight camera.	10
3.2	Illustration of the mixing process	10
3.3	Configuration 1.	10
3.4	Configuration 2.	10
4.1	Example of modulator structure.	12
4.2	Quantum well without and with applied electric field	13
4.3	Reflectance profile	14
4.4	Four modulators connected by gold wires to a PCB.	14
4.5	Example of a measured I-V characteristic	15
4.6	Picture of the characterization setup	15
4.7	Modulator B1-2000-R absorption profile at $\theta = 15^\circ$	16
4.8	Modulator B1-1000-L absorption profile at $\theta = 22.5^\circ$	16
4.9	Modulator B3-1000-R absorption profile at $\theta = 30^\circ$	17
4.10	Modulator B3-2000-R absorption profile at $\theta = 45^\circ$	17
4.11	FP cavity resonance vs illumination angle	18
5.1	Measured signal illustrating the three unknown variables	21
6.1	Cut-off frequency versus modulator size	25
6.2	Minimum and maximum illumination powers	27
6.3	Measured and estimated distance resolution versus received optical power	28
7.1	Pictures of the experimental setup	31
8.1	Laser output signal for a square wave modulation at $f_{mod} = 15$ MHz.	32
8.2	Non-linearity effects	33
8.3	Picture of the measurement scale	34
8.4	2D picture taken with the 3D time-of-flight camera	35
9.1	Data acquisition and computation.	37
9.2	Short range measurements.	38
9.3	Long range measurements.	38
9.4	Calibrated measurements.	38
9.5	Repetability estimation: example	39

Contents

1	Introduction	4
1.1	Background and motivation	4
1.2	Contents	4
2	3D Time-of-flight imaging	6
2.1	Principle	6
2.2	Commercialized cameras	7
3	Proposed design for a 3D camera	9
3.1	Shutter	9
3.2	Configuration	10
4	Choice of modulator	12
4.1	Theory of quantum well electro-absorption modulators	12
4.2	Assembly and I-V tests	13
4.3	Characterization experiments	15
4.4	Results, limitations and selection	17
5	Signal processing methods	20
5.1	Homodyne method	20
5.1.1	Principle	20
5.1.2	Application	21
5.1.3	Advantages and limitations	22
5.2	Heterodyne method	22
5.2.1	Principle	22
5.2.2	Application	23
5.2.3	Advantages and limitations	23
5.3	Choice of processing method	24
6	Theoretical performances	25
6.1	Driving frequency and measurement range	25
6.2	Intensity received on the sensor	26
6.3	Depth resolution	27
7	Setup details	30
7.1	Material	30
7.2	Distances computation	30

8 Experiments	32
8.1 Preliminary checks	32
8.2 Distance measurements	33
8.2.1 Parameters	33
8.2.2 Image acquisition	34
8.2.3 Problems encountered and solutions found	34
8.2.4 Limitations	35
9 Results and discussion	37
9.1 Measurements results	37
9.2 Evaluation of performances	39
9.2.1 Repetability	39
9.2.2 Accuracy	40
9.2.3 Global resolution	40
9.3 Limitations and solutions: summary	41
10 Conclusion and perspectives	42
Acknowledgements	44
Bibliography	45
A List of material specifications	47
B Program for distance computation	49

Chapter 1

Introduction

1.1 Background and motivation

Compared to our 3D environment, 2D images lack an important feature: depth. As a consequence, elements at different distances seem to be superimposed in the 2D picture. An accurate analysis of a scene requires methods to distinguish between the different objects present. This can be a very heavy computation task for 2D imaging. 3D imaging is a technique that adds range (depth) information to conventional 2D images, and therefore leads to a more reliable interpretation.

3D imaging systems are of high interest for a wide range of applications in security, defense, industry as well as entertainment. Previously, 3D measurement has been realized with triangulation systems, determining the location of a point by measuring angles to it from known points at either end of a fixed baseline. But these systems present many limitations (shadow or contrast effects, computational time, cost, portability, etc.). The 3D time-of-flight imaging technique, in which the time it takes for the light to travel from a scene to the camera is measured, is able to give fast and accurate values of an object's distance. However, the existing systems using this technology are complicated and thus costly. A model of camera using cheaper technologies would be perfect to meet the market's needs.

In this context, the purpose of this thesis is to experimentally evaluate a simple and low-cost solution for 3D time-of-flight imaging, with a conventional CCD camera and a fast optoelectronic shutter. For the shutter, key component of the system, a GaAs modulator designed by Acreo is used. Eventually, this thesis work also draws the lines for improvements or possible future work with similar technologies.

1.2 Contents

In this project, a solution to this problem and a demonstrator are presented. After introducing the background and the motivations behind the project in chapter 1, the 3D time-of-flight principle is explained in chapter 2. In chapter 3, a design for a camera is proposed. The choice made for the fast optoelectronic

shutter is detailed in chapter 4. Different possible signal processing techniques to accurately extract 3D information are discussed in chapter 5, and one is selected for the demonstrator. In chapter 6, the expected theoretical performances are calculated for the experiments. The final demonstrator (chapter 7) and the experiments carried out (chapter 8) are described. The performances of the solution are evaluated in terms of accuracy, repeatability and global resolution in chapter 9. Eventually, in chapter 10, recommendations for future work are made.

Chapter 2

3D Time-of-flight imaging

2.1 Principle

A classical camera records the intensity of a scene on a 2D array sensor. To get a 3D image, information about the distance from the camera to the objects is needed. A way to access this information is to consider the propagation of the light from an object to its image on the camera. If the propagation time between two points is known, the distance between them can be deduced instantly. This way, using an active illumination of a scene and its reflection on the objects, the distance can be recorded in every pixel of an image sensor. This method is called time-of-flight 3D imaging.

The direct way to measure the distance is to send a pulse of light towards the scene to image. The light is reflected on the objects and sent back to the camera. The distance is then directly calculated from the time delay between the emitted pulse and the pulse received [1].

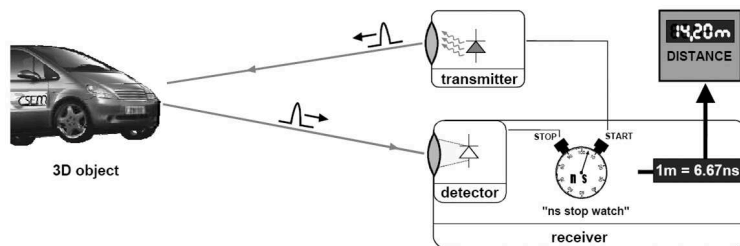


Figure 2.1: Time-of-flight principle with a pulsed light (from [2]).

The method used in this work is based on the same principle, but uses an amplitude-modulated continuous wave. Easier to implement, this method is also more adapted to the technologies available.

The light source is, in this method, modulated in a continuous wave. When the light reflected on an object reaches the detector, it is time-delayed due to the propagation, which results in a phase-shift compared to the initial modulation signal. From the phase-shift, the propagation time and then the distance can

be deduced.

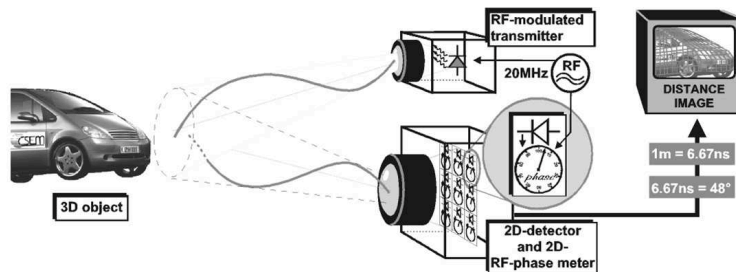


Figure 2.2: Time-of-flight principle with an AM light (from [2]).

The use of a periodically-modulated continuous wave presents one disadvantage compared to the pulse of light. The cyclic nature of the modulation signal implies that the camera cannot differentiate between two objects spaced by a distance $\lambda/2$ (λ being the wavelength of the light), because the two reflected lights present the same phase-shift when they reach the detector. In terms of phase-shift, there is a π -ambiguity. The consequence is that, in the absence of ambiguity range processing, the camera only pictures correctly "slices" of the scene. The different "slices" appear superimposed. Details and a solution to this problem are found in Chapter 5.

2.2 Commercialized cameras

About ten 3D time-of-flight cameras are already commercialized. To the best of the author's knowledge, they all work in the near-infrared range (around 850 nm) and they are based on three different sensors.

- PMDtechnologies sensor (CMOS technology) [3]
- Mesa imaging sensor (combine CCD/CMOS technology) [4]
- Canesta sensor (CMOS technology) [5]

Different technologies are also used for the RF-phase meter: either internal to the sensor with 2-tap pixels for example, or external with a shutter.

The time-of-flight cameras usually cost between \$4,000 and \$12,000 at the time this report is written (January 2011) [6]. Table 2.1 shows the typical specification of today's cameras.

Model	Modulation	Range	Accuracy	Repetability
PMD[vision]® O3	25 MHz	6 m	NC	5 to 74 mm
Mesa SR4000 (1)	15 MHz	10 m	15 mm	6 to 9 mm
Mesa SR4000 (2)	30 MHz	5 m	10 mm	4 to 7 mm
Fotonic B40	44 MHz	10 m	5 mm	1 to 2 cm

Table 2.1: Examples of time-of-flight camera specifications (from [7], [8] and [9])

Chapter 3

Proposed design for a 3D camera

The proposed time-of-flight camera requires six basic elements.

- A light source
- A shutter system
- A CCD/CMOS sensor
- A signal generator device
- Some optical elements
- Some software

As shown in figure 3.1, a signal generator modulates the light source and the shutter at typical modulation speeds of tens of MHz. The amplitude-modulated light source illuminates a scene and the light is reflected on the objects within the field-of-view back to the camera. With some optics, the light propagates to the shutter and is directed to the sensor. Depending on the phase-shift between the returning light and the modulation signal of the shutter, the amount of light that is transmitted varies, relating the light brightness on the sensor directly to the phase-shift. Figure 3.2 illustrates this idea in the particular case of a square-wave modulation of the light and the shutter. In this configuration, the received intensity is simply linearly dependant to the range.

The software records images and compute distances thanks to the intensity variations between the different images.

3.1 Shutter

The key component of such systems is the shutter unit. It has to be modulated at high frequencies (typically 10 to 100 MHz for good resolution) with a short rise/fall time and present a good on/off contrast. Such requirements make good time-of-flight camera difficult to realize and expensive. A few years ago, Acreo has designed and produced opto-electronic components that fulfil these

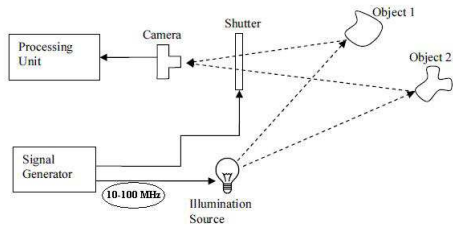


Figure 3.1: Basic design of a 3D time-of-flight camera.

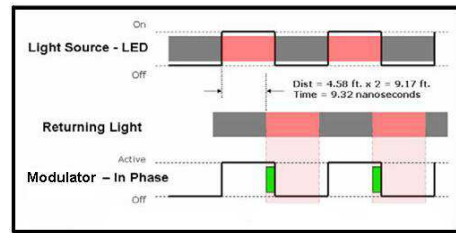


Figure 3.2: Illustration of the mixing process between the returning light and the shutter (from [10]).

conditions. The surface-normal quantum well electroabsorption modulators developed by S. Junique *et al* [10]. can be driven with a small amplitude voltage modulation to hundreds of MHz, and has shown in previous studies modulation contrasts close to 300:1.

The modulation frequency is nevertheless limited by the size of the modulator. Typically, the cut-off frequency of such components is inversely proportional to the area of the active surface. As shown in Chapter 6, for a cut-off frequency of 15 MHz, one must choose a modulator of size around 1 mm^2 or smaller. In the present project, the choice was made to work with a modulator of 1 mm^2 , 4 mm^2 or 0.25 mm^2 . A bigger modulator would limit too much the performances, but a smaller one would require advanced optics.

3.2 Configuration

The modulator described above works in reflection. It is chosen large enough to use simple optical elements. Given those facts, they are two possible interesting configurations for the demonstrator.

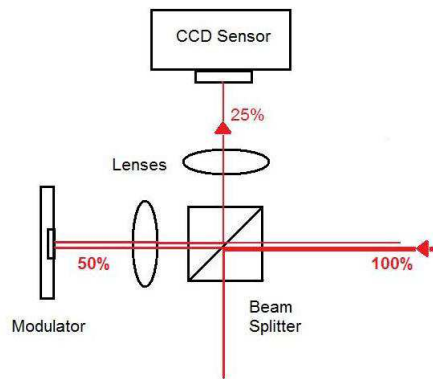


Figure 3.3: Configuration 1.

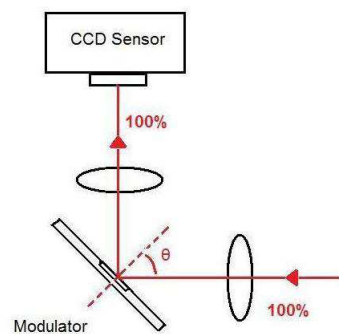


Figure 3.4: Configuration 2.

The main advantage of the first configuration is a normal reflection of the light. Because the previous experiments showing really good contrasts were carried out with an illumination angle close to zero, this configuration is likely to show similar results. Moreover, the image is normally focused on the surface. The main drawback is that the only light source adapted and available for this project gives low illumination powers. Configuration 1 was tested with a mirror instead of a modulator. The resulting image on the sensor was already weak despite an almost perfect reflection. For this reason, the second configuration was preferred.

With the second configuration, the use of a beam splitter is avoided. The optimum reflection angle depends on the modulator's characteristics. Some preliminary experiments were carried out to determine an optimized angle and its associated contrast.

Chapter 4

Choice of modulator

4.1 Theory of quantum well electro-absorption modulators

The ultrafast shutter considered for the 3D camera is a surface-normal multiple quantum well electroabsorption modulator based on GaAs material. Electroabsorption is the physical phenomenon by which the optical absorption in a medium can be controlled with an electric field. This effect is strong in modulators with multiple quantum wells (MQW), which make them convenient for an application to 3D time-of-flight imaging.

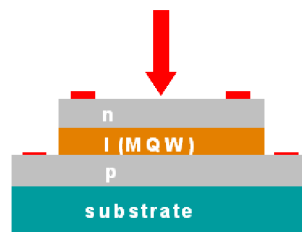


Figure 4.1: Example of modulator structure.

A quantum well is a thin layer of a narrow-bandgap material inserted between two layers of a wider-bandgap one. Due to the small size of the wells, discrete levels of energy appear. When absorption can occur, an electron is promoted from its hole energy in the valence band to an electron level of same parity in the conduction band. But there is also absorption when an electron does not quite reach its level in the conduction band, and instead remains bound to the positive vacancy it has left in the valence band. This electron-hole entity can be seen as a hydrogenoid atom, with the negative and positive charges orbiting around their center of gravity. This is called an exciton. It is stable and likely to exist during a measurable amount of time. There are actually two of these exciton absorption peaks in multiple quantum well modulators.

An interesting property of the quantum wells is that, when an electrical field is applied, an important shift in their bandgap energy is observed. This is called the Quantum-Confined Stark Effect (QCSE). The QCSE shifts the absorption peaks of the quantum wells towards longer wavelengths.

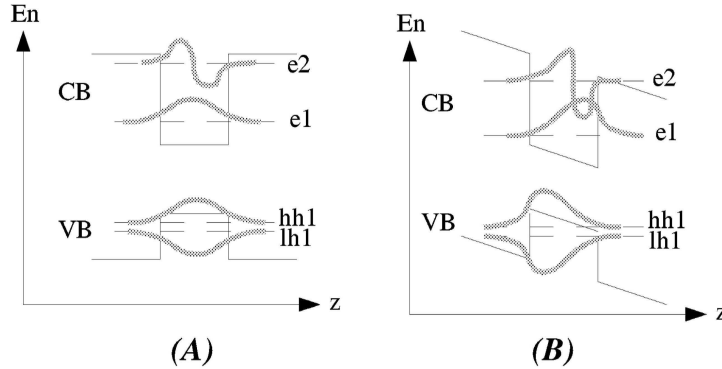


Figure 4.2: A quantum well without (A) and with (B) applied electric field. VB and CB are the valence and conduction bands; E_n denotes the electron potential energy; z is the growth direction of the layer stack; e1 and e2 are the first and second energy levels; hh1 and lh1 are the first heavy hole and light hole energy levels.

This absorbing medium is embedded in an asymmetric Fabry-Perot resonator. The reflectance is then minimal at the resonant wavelength. This is the cavity absorption peak[10].

To use the cavity as a modulator, the cavity absorption peak must be slightly blue-shifted compared to an excitonic peak. The quantum well exciton peak can then be alternatively shifted towards the cavity resonance by applying a voltage. In the first state, when no voltage is applied, there is low absorption at for the operating wavelength. Most of the light is reflected on the modulator. In the second state, a voltage is applied, shifting the excitonic peak towards the cavity resonance. The absorption peak in the cavity is then strong and less light is reflected on the modulator. Figure 4.3 illustrates this principle.

4.2 Assembly and I-V tests

For the reasons detailed in Chapter 6, the choice was made to select modulators of a size around 1 mm^2 . We took 12 modulators, with similar sizes: 4 modulators of area 4 mm^2 , 4 of 1 mm^2 and 4 of 0.25 mm^2 . Due to the nature of the fabrication process, the modulators do not all present the same resonance and exciton peaks. Thus, it is necessary to measure their characteristics before using them.

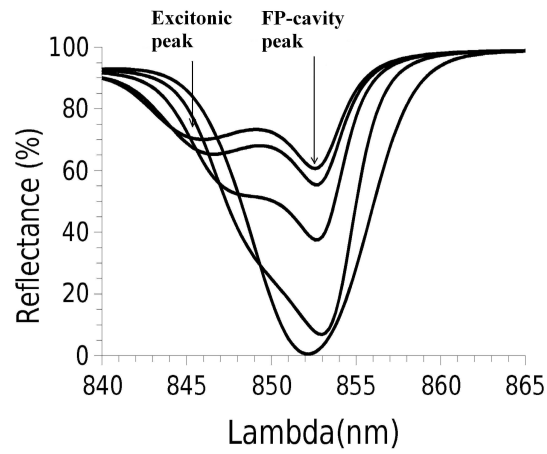


Figure 4.3: Reflectance profile of a quantum well electro-absorption modulator with different electric fields applied.

In order to electrically drive the modulators, they are separated by blocks of four, glued to a printed circuit board (PCB) and bound to the conductive pathways by gold wires as shown in figure 4.4.

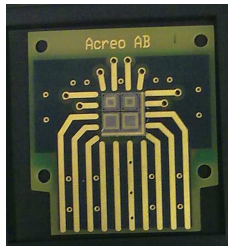


Figure 4.4: Four modulators connected by gold wires to a PCB.

The first step after assembling is to measure the intensity vs. voltage (I-V) characteristics of the modulators. They work as p-n junctions with reversed bias. Figure 4.5 shows an example of such characteristic.

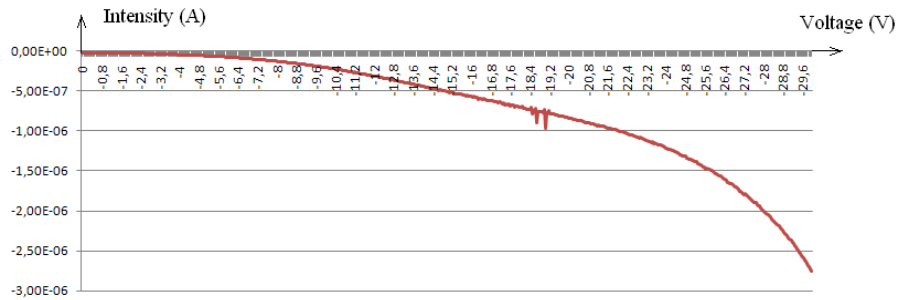


Figure 4.5: Example of a measured I-V characteristic. Modulator used: B1-1000-R.

The conclusions of the I-V tests are that 10 modulators out of the 12 tested present a breakdown voltage higher than 15 V and are suitable for the experiments.

4.3 Characterization experiments

In order to characterize the modulators, i.e. to localize the different absorption peaks and evaluate their depths, reflectance measurements were performed with a spectrometer. A pigtailed SuperLuminescent Diode (SLD) in the 820 nm-865 nm range was connected to a fibred collimator to illuminate the device. The reflected beam was coupled back to a fiber through another collimator and sent to an Optical Spectrum Analyser (OSA).

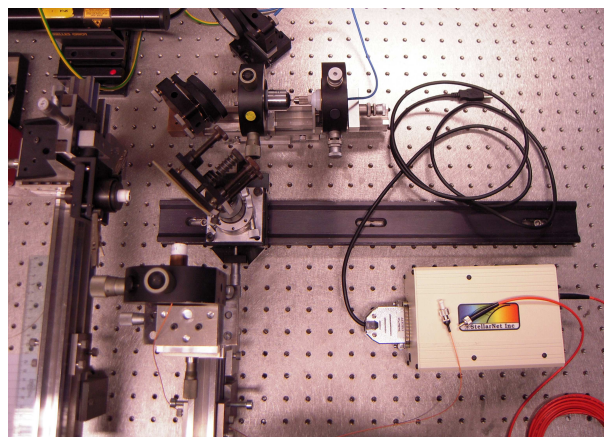


Figure 4.6: Picture of the characterization setup; to the left, the optical fiber+collimator emitting the light from the SLD, the modulator plate (without electrical connection here) and the receiving collimator+optical fiber; to the right, the OSA.

Measurements were carried out with beam incidence angles of $\theta = 15^\circ$, $\theta = 22.5^\circ$, $\theta = 30^\circ$ and $\theta = 45^\circ$. The beam collimator was focused on the device and formed a 1 mm luminous spot. The reflection curves were measured with the OSA for voltages from 0 V to 15 V, then normalized with the SLDs characteristic to reveal the different absorption peaks. Figure 4.7, figure 4.8, figure 4.9 and figure 4.10 give examples of characteristics obtained for each measurement angle.

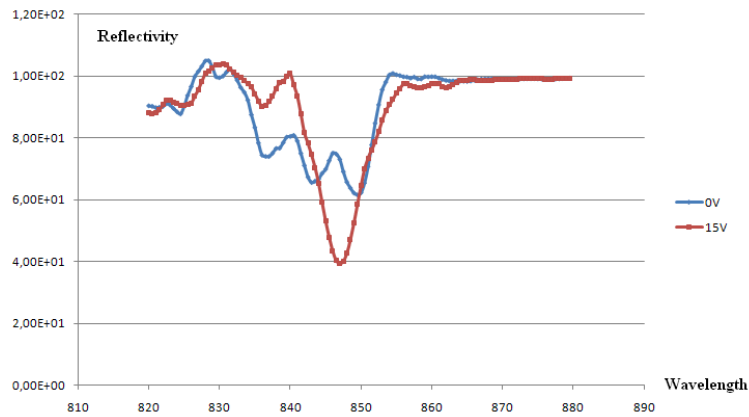


Figure 4.7: Modulator B1-2000-R. Illumination angle $\theta = 15^\circ$. Absorption as a function of the wavelength.

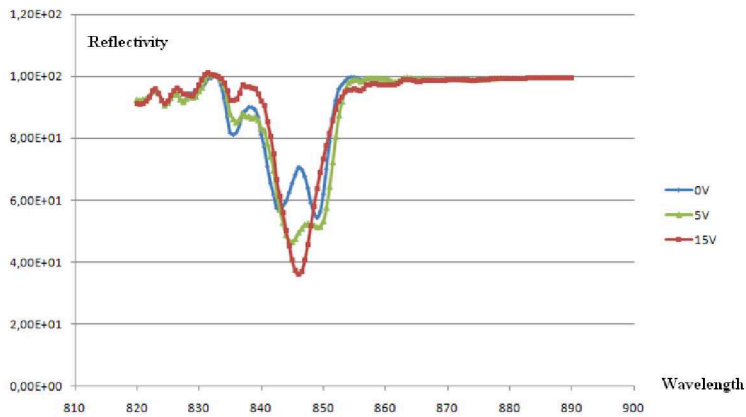


Figure 4.8: Modulator B1-1000-L. Illumination angle $\theta = 22.5^\circ$. Absorption as a function of the wavelength.

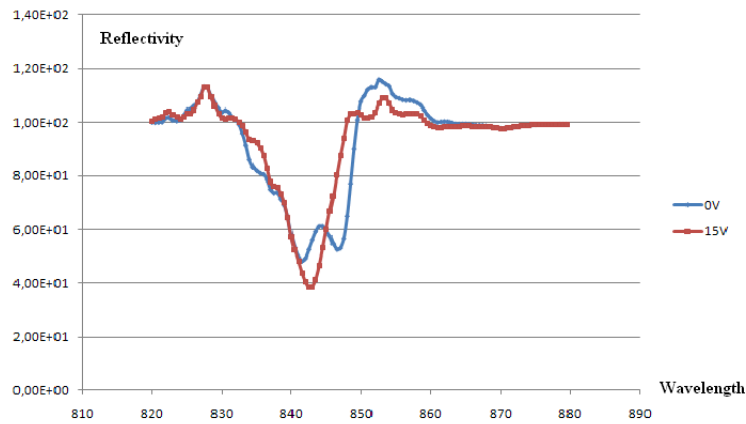


Figure 4.9: Modulator B3-1000-R. Illumination angle $\theta = 30^\circ$. Absorption as a function of the wavelength.

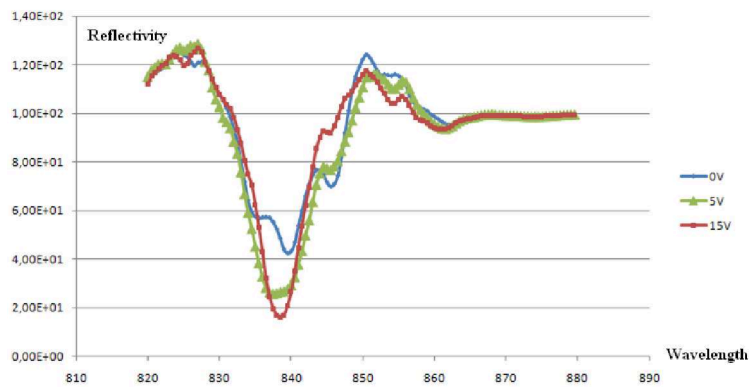


Figure 4.10: Modulator B3-2000-R. Illumination angle $\theta = 45^\circ$. Absorption as a function of the wavelength.

4.4 Results, limitations and selection

The analysis of the curves leads to the following observations.

- Without applied voltage ($U = 0 \text{ V}$)
 - Two excitonic peaks appear on all devices at 836 nm and 842 nm.
 - The position of the absorption cavity peak varies from one modulator to another, due to the fabrication process and the beam incidence angle.
 - As the beam incidence angle increases, the cavity absorption peak is shifted towards shorter wavelengths (figure 4.11).
- With applied voltage ($U = 15 \text{ V}$)

- The exciton peaks are shifted towards longer wavelengths.
- The absorption minimum decreases.

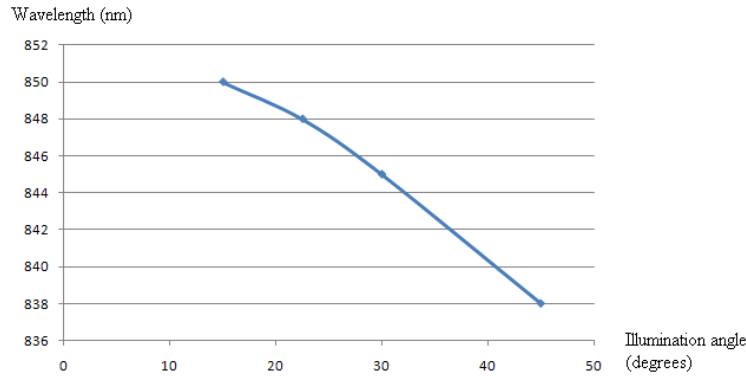


Figure 4.11: Position of the Fabry-Perot cavity resonant absorption peak versus illumination angle.

The cavity resonance peak without applied voltage is located around 850 nm for incident angle $\theta = 15^\circ$ (see figure 4.7), at the right of the first exciton peak. It decreases to about 848 nm for $\theta = 22.5^\circ$ (figure 4.8), and 845 nm for $\theta = 30^\circ$ (figure 4.9). The result is an absorption peak with applied voltage located around 846 nm for these illumination angles. For $\theta = 45^\circ$ (figure 4.10), the cavity peak is located at the left of the first exciton peak, but still at the right of the second exciton peak, leading to an absorption cavity with applied voltage around 837 nm.

The modulation depth varies in accordance to the position of the cavity peak and the voltage applied. With $U = 15$ V, the absorption is close to 90% for some measurements at $\theta = 45^\circ$, but the corresponding absorption without applied voltage is also important, leading to a good contrast but a small difference in modulation amplitude. For the other measurements, the absorption does not increase much at $U = 15$ V, staying below 65%, but is down to 30% at $U = 0$ V, creating a greater difference in amplitude.

The choice between those two cases is made considering the post-processing of the images and the illumination. In the first case, the absorption is important even with no voltage applied, which means less intensity reaching the sensor, and thus loss of precision in the distance measurement. In the second case, the absorption is low when no voltage is applied, but it does not increase a lot with voltage applied. This implies that, when driving the modulator, the mode "off" still let some light through. Thus, the signal will have an offset, but this offset can be calculated and, if not too important, will have a limited impact on the distance measurements.

Because our illumination is not powerful, we chose to favor the second option. Moreover, it is likely that the contrast in absorption proves to be more

important than first measured as undesirable reflections can occur on the sides of the modulator, highly reflective.

Thus, the modulator employed eventually is B1-1000-L¹ at $\theta = 22.5^\circ$. This angle has been chosen both for the good amplitude modulation it offers and for ease of mounting. The corresponding wavelength is $\lambda = 846$ nm.

¹Each modulator is referred to as Modulator X-S-P(-C), where X is the initial location on the processed chip, S is the side length or the radius in μm , P is its location on the 4-modulators block and C is indicated when the modulator has a circular geometry.

Chapter 5

Signal processing methods

The optical signal received by the camera has to be computed to extract depth information. To do so, three main types of modulation are currently employed: pulsed, homodyne and heterodyne. Because the choice was made to operate with a continuous wave, the pulsed solution is not considered. The homodyne method is fully explained, and the heterodyne method is presented for possible future work.

5.1 Homodyne method

5.1.1 Principle

Homodyne systems operate with an illumination light and a shutter, both amplitude-modulated. In this situation, the propagation delay is encoded in the phase change of the returning light compared to the emitted one. At the modulator level, the light signal is "mixed" with the shutter's signal. For a modulation in sine-wave $s(t) = K\cos(\omega t)$, the returning light is $s_1(t) = AK\cos(\omega t + \varphi)$ and the driving signal at the shutter $s_2(t) = K\cos(\omega t + \omega\tau)$, where φ is the phase-shift due to the light propagation time and $\omega\tau$ represents the relative phase difference between the illumination signal and the shutter signal. The mixing product $s_1.s_2$ is

$$I(t) = \frac{1}{2}AK[\cos(2\omega t + \varphi + \omega\tau) + \cos(\varphi + \omega\tau)]$$

and results in a time averaged signal

$$I = \frac{1}{2}AK\cos(\varphi + \omega\tau).$$

Thus, the intensity received by the sensor differs for different phase-shifts.

Deriving the range from the brightness of the images requires some computation. The homodyne method often uses several measurements with two or more different values of the relative phase $\omega\tau$ between the illumination and the

shutter modulation signals. From those values, the phase-shift and then the distance are calculated.

5.1.2 Application

A light source is intensity-modulated at a high frequency, usually between 10 MHz and 100 MHz, and illuminates a scene. Objects within the field reflect the light back towards the imaging system. Due to the time taken to execute a round-trip, the phase angle φ of the light source modulation signal is retarded according equation 5.1, where f_{mod} is the modulation frequency, d is the distance to the object, and c is the speed of light [12].

$$\varphi = \frac{2\omega d}{c} = \frac{2(2\pi f_{mod})d}{c} \quad (5.1)$$

If the incoming light is recorded over a large number of modulation periods, the signal is averaged and the received intensity depends on $\cos(\varphi)$. In order to deduce the phase-shift φ , the amplitude A and the offset B from the recorded signal, the 4-buckets method is applied: Four images are recorded, with each time a different phase-shift $\omega\tau$ introduced between the shutter and the light source ($\omega\tau_1 = \omega\tau_0 + 90^\circ$, $\omega\tau_2 = \omega\tau_0 + 180^\circ$, $\omega\tau_3 = \omega\tau_0 + 270^\circ$) [13]. The four images then have a different intensity, as illustrated in figure 5.1.

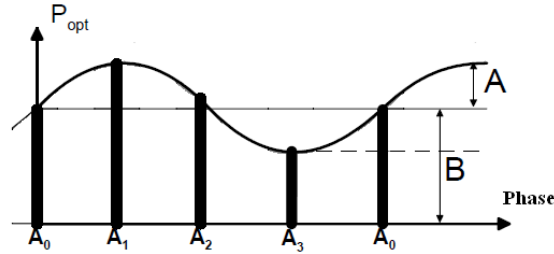


Figure 5.1: Measured signal illustrating the three unknown variables: amplitude A , offset B and phase φ .

The four measurements allow the three unknown variables to be determined from the following equations:

$$A = \frac{\sqrt{(A_0 - A_2)^2 + (A_1 - A_3)^2}}{2} \quad (5.2)$$

$$B = \frac{A_0 + A_2 + A_1 + A_3}{4} \quad (5.3)$$

$$\varphi = \arctan \frac{A_0 - A_2}{A_1 - A_3}. \quad (5.4)$$

By measuring the phase angle of the modulation envelope using the equation, substituting into equation 5.1 and rearranging, the distance d is deduced:

$$d = \frac{c\varphi}{4\pi f_{mod}} \quad (5.5)$$

Due to the periodicity of the modulation, the distance is known modulo $2\pi c/(2\omega)$. This principle can also be applied with other waveforms: triangle, square... although the presence of high-order harmonics has an impact on the calculations (see next section).

With this method, by using a light source, a fast opto-electronic shutter and a sensor array, all points in the scene can be acquired simultaneously, which enable fast range acquisition for applications requiring a high resolution range image.

5.1.3 Advantages and limitations

The main advantage of this method is its ease of application. It does not require elaborate electronics and the computation is fast. As a consequence, it is suitable for real-time imaging and cost-efficient.

But it is not free of defects. Because of the nature of phase change, range ambiguities occur at multiples of half of the wavelength of the modulation signal. These ambiguities can be resolved by performing two measurements with differing modulation frequencies [14].

For homodyne systems, pixel brightness is affected by background lighting and differences in objects' reflectance. The background lighting reduces the number of available digitization levels to encode the phase and the amplitude of the signal, thus reducing the resolution. If the objects have very different reflectivities, some can be over-exposed and saturate the sensor (hence giving false distance values) while other are under-exposed and do not reflect enough light. Procedures are required to limit the impact of those phenomena, for example optical band-pass filters are often used [15].

Moreover, in the case where the signal use is not a sine wave, harmonics are added to the fundamental frequency, resulting in an error in the measured phase. This error is cyclic, as shown in experimental results found by A.A.Dorrington *et al.* It is possible to limit the effect of these non-linearities by some pre-processing or post-processing methods.[12] [13] [16]

5.2 Heterodyne method

5.2.1 Principle

Heterodyne systems are different from homodyne systems in that the modulation frequencies applied to the illumination and shutter differ slightly in fre-

quency. This means the mixing process at the shutter produces a beat frequency equal to the difference between the modulation frequencies. The phase of the collected light modulation envelope (which is proportional to propagation delay and hence range) is also encoded in the beat signal. The image captured by the camera therefore appears to be "flashing", and objects at different distances flash at different times. Range information for each pixel can be determined by acquiring a video sequence of the scene and calculating the beat signal phase or frequency (over time) for each pixel (explanation from [11]).

5.2.2 Application

The simplest heterodyne implementation uses fixed modulation frequencies with a known difference, and relies on measuring the phase change of the beat signal to determine range. With f_1 the frequency of the modulated light and $f_2 = f_1 + \delta$, for δ small, the frequency of the fast shutter. The light received after mixing at the shutter is:

$$\cos(2\pi f_1 t + \phi) * \cos(2\pi f_2 t) = \cos(2\pi |f_1 - f_2| t + \phi) + \text{high-frequency terms}, \quad (5.6)$$

where only the low frequency term on the right-hand side is received at the camera. It consists of a beat frequency $\delta = |f_1 - f_2|$ with a phase-shift, ϕ , namely the phase-shift due to the time of flight. Thus, to measure the range to a point of a scene imaged in any one particular pixel of the camera, one samples the scene for at least a complete cycle of the heterodyne beat and then calculates the phase of the received signal. Again it is then easy to obtain the distance to the scene from the phase (explanation from [17]).

Another type of heterodyne approach is to use a Frequency Modulation Continuous Wave (FMCW). There, the modulation signals are swept in frequency, which causes the beat signal to vary in frequency as a function of the propagation delay of the light. In this case, an analysis of the frequency of the beat signal determines the range.

To record the beat signal, video cameras are necessary, but they are often limited to a 10 or 100 Hz frame rate. Therefore, the beat signal δ must be set at a maximum of a few singles or tens of Hertz in order to respect the Nyquist sampling frequency criteria. It is then important to ensure the stability of the two modulation signals with sub-Hertz precision. For this purpose, frequency locked generators are convenient [17]. With the frequency locked signal generators, one can also generate a synchronization signal to the camera. When the camera frame clock is synchronized, the beat signal is recorded exactly within one period of the beat signal, which is the ideal situation for the phase measurement, as it avoids some additional post-processing.

5.2.3 Advantages and limitations

The heterodyne method has a number of significant advantages over the homodyne method. The range is encoded in the variation over time of the intensity, independently from absolute or average intensity, and is thus not directly affected by background illumination and objects' reflectivities. However, signal-

to-noise ratio impacts on measurement precision, so strong background lighting or highly contrasted objects can indirectly influence the precision. It follows from this property that the objects reflectivity and the background illumination can also be determined independantly, respectively from the amplitude of the beat signal and from its mean value. The heterodyne method is also much less sensitive to digitization limits than the homodyne method. Moreover, the presence of harmonics on the light and shutter signal do not adversely affect the phase measurement, thus nonlinear responses are easily tolerated. (explanation from [11]).

But these good properties have a cost. Generating two stable signals with a difference of 7 or 8 orders of magnitude lower than the fundamental frequency can be tricky to achieve in practice. If the synchronization is not perfect, some post-processing is needed, for example a zero padding procedure [17] can be used. To synchronize the video frame clock also complicates the setup, and if not synchronized, adds an offset to the signal. The scene then requires an object at a known distance to be accurately analysed.

5.3 Choice of processing method

In this project the homodyne method is applied. Because it is simpler to implement with the available equipment, this method was considered more suitable for a first demonstrator. Nevertheless, the heterodyne method presents many advantages compared to the homodyne method (tolerance to background illumination, reflectivity inconsistencies, presence of harmonics, digitization limits). These would make the former an interesting candidate for further improvements.

Chapter 6

Theoretical performances

6.1 Driving frequency and measurement range

The frequency of the modulator is, as mentioned previously, size-dependant. The smaller it gets, the easiest it is to drive it at high frequencies. This property derives from the dependance of the capacitance of the modulator to its area. The cut-off frequency at -3dB, f_{-3dB} , is inversionally proportional to the product resistance(R)*capacitance(C):

$$f_{-3dB} = \frac{1}{2\pi RC} \quad (6.1)$$

$$C = \frac{\varepsilon\varepsilon_r A}{e} \text{ (thin-plate capacitance model)} \quad (6.2)$$

The resistance of can be assumed to be weak, the equivalent resistance of the system then being the resistance of the electrical connections: $R = 50 \omega$. The result is shown in figure 6.1.

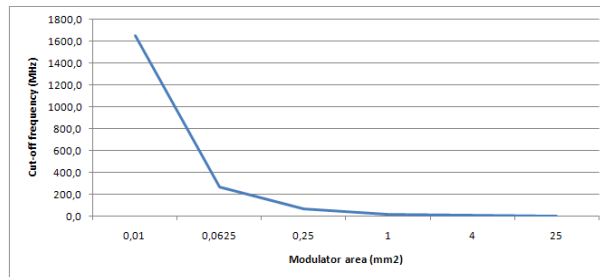


Figure 6.1: Cut-off frequency versus modulator size

The measurement range of a time-of-flight camera depends directly on the modulation frequency used. Some values are given in table 6.1 as examples, that were calculated using equation 5.5.

Frequency (MHz)	1	2	3	5	10	15	20	30	40	50	100
Range (m)	150	75	50	30	15	10	7.5	5	3.75	3	1.5

Table 6.1: Examples of measurement range for different modulation frequencies.

6.2 Intensity received on the sensor

Time-of-flight cameras use active illumination. Hence, it is important to determine the requirements for the optical power of the light source.

It is assumed that the object is a Lambert reflector, i.e. the intensity distribution of back-scattered light does not depend on the illumination angle. The reflected intensity decreases with the cosine of the observation angle with respect to the surface normal. The reflection coefficient has values between zero and one for Lambert reflectors (=1 for a white sheet of paper). The required power of the light source is then¹:

$$P_{lightsource} = \frac{N_e \frac{A_{image}}{A_{pixel}} hc}{\rho \left(\frac{D}{2R}\right)^2 k_{lens} QE(\lambda) \lambda T_{int}} \quad (6.3)$$

N_e	number of electrons per pixel	D	lens aperture
A_{image}	image size in sensor plane	R	distance to object
A_{pixel}	light sensitive area per pixel	k_{lens}	losses of optical elements
h	Planck's constant	QE(λ)	quantum efficiency
c	speed of light	λ	wavelength of light
ρ	reflectivity of object	T_{int}	integration time

For an exemple with conditions close to the ones in the experiments, let's take an image that covers the whole sensor, $A_{image} = 4 \text{ mm}^2$, a lens aperture of 1 cm, an object at a distance of 1 m, losses of lenses around 0.8 and in the modulator around 0.52 (on average), a quantum efficiency of 0.8 at $\lambda = 846 \text{ nm}$. The object presents a reflectivity around 0.7 and the reading frequency of the pixels is $f_{pixel} = 1 \text{ MHz}$.

Then, in order to get an image between noise threshold (5 gray levels, ie $5 * \frac{E_{saturationpixel}}{256} QE(\lambda) \frac{\lambda}{hc} = 5 * 884$ electrons) and saturation limit (255 gray levels, ie $255 * 884$ electrons), the necessary power is:

$$0.3 \text{ mW} < P_{lightsource} < 14.5 \text{ mW}.$$

One important parameter when choosing the power of the light source is the distance of the object. As the equation 6.3 shows and as figure 6.2 illustrates on a log-scale, the illumination power needed is proportionnal to the square of the distance. When determining the range measurement, one must also take into account the amount of light that will be reflected back into the sensor.

¹Detailed calculations in [19].

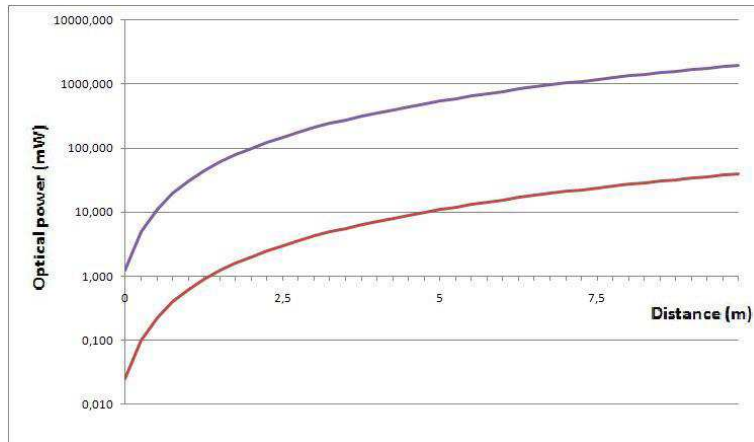


Figure 6.2: Illustration of minimum and maximum powers for the illumination unit as a function of the distance.

6.3 Depth resolution

The depth resolution of a time-of-flight camera is limited by number of disruptive effects and noises.

The digitization of the signal is an important limiting factor. For a 8-bit analog-to-digital converter, the signal is coded on 256 levels. For a modulation in square wave, the mixing at the shutter gives a triangle with the same period as the modulation signal. In this case, with a linear response of the sensor to the received intensity, 1 gray level represents 0.7° . With a modulation frequency $f_{mod} = 15$ MHz, digitization thus lead to a limit of the camera resolution of 1.9 cm that can only be improved by increasing the number of digitization levels or increasing the modulation frequency.

As a direct consequence, ambient light is also a limitation of the system because it reduces the number of available levels.

Noises mainly originate from the light source and the photocharge conversion. The principal noises of the light source are the photon shot noise and the Speckle effect. Photocharge conversion noise is composed of several contributions, among them reset noise, $1/f$ noise (flicker noise), thermal noise and dark current noise. All these contributions increase with temperature. To these can be added the ambient light that not only reduce the number of digitization levels but also increases the quantum noise.

Photon shot noise is a very important noise source since it is the only one that cannot be suppressed. Moreover, since photon shot noise increases with the number of incoming photons, it eventually predominates over all other noise sources and hence becomes the limiting factor to the effective signal-to-noise ratio. Equation 6.4 gives an estimation of the depth resolution due to photon

noise [19]:

$$\Delta L = \frac{L}{360^\circ} \Delta\varphi = \frac{L}{\sqrt{8}} \frac{\sqrt{B}}{2A} \quad (6.4)$$

- L: Non-ambiguity distance range ($L = \frac{\lambda_{mod}}{2} = \frac{c}{2f_{mod}}$).
- A: Modulation amplitude, i.e. the number of photoelectrons per pixel generated by the AC component of the modulated light source.
- B: Offset or acquired optical mean value, i.e. the number of photoelectrons per pixel generated by incoming light of the scenes background and the mean value of the received modulated light.

For example, for $A = 22,650$ electrons and $B = 79,600$ electrons (evaluations based on experimental observations of intensity values for A and B, converted to number of electrons), the depth resolution is:

$$\Delta L = 2.2 \text{ cm.}$$

This range accuracy, which can only be improved by averaging, is the absolute limit of a range sensor working with the 4-buckets homodyne method.

Moreover, A is dependant on the illumination power. Indeed, A can be expressed as a function of the optical mean power or the total number of photoelectrons per pixel generated by the modulated light source PE_{opt} : $A = C_{light\ mod} * C_{shutter\ mod} * PE_{opt}$, where $C_{light\ mod}$ and $C_{shutter\ mod}$ are the modulation contrasts (in percentage) of the light source and the shutter. Consequently, the depth resolution is inversely proportional to the received power as shown in figure 6.3, example from [19]. For lower power, i.e. longer range, the resolution can thus decrease very fast.

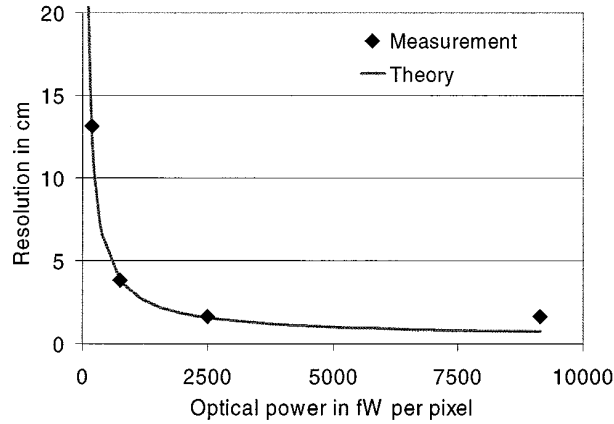


Figure 6.3: Measured and estimated distance resolution versus received optical power per pixel (from [19]).

An additional limitation arises from the nature of the modulation signals. As mentioned before, the homodyne method works ideally with perfect sine waves. In practice, the signals used are likely to contain additional harmonics.

The measurement is altered by the high harmonics and show some discrepancies for certain values of the phase-shift. This effect is not treated theoretically because the harmonic content of the modulation signals is not precisely known, but it will be characterized experimentally (see Chapter 8).

Chapter 7

Setup details

7.1 Material

A setup was assembled to be used as a demonstrator and to evaluate the performances of a simple and low-cost time-of-flight imaging system. Among the components of the system are¹:

- A tunable diode laser in the near-infrared range with optical output ≤ 10 mW (wavelength-dependant).
- Classical lenses of chosen focal lengths.
- Diffuser made of adhesive tape.
- A CCD camera 128x128 pixels with adjustable integration time.
- A computer equipped with a software to drive the camera and record pictures (software developed by S.Junique [10]).

To complete the setup, some additional elements were selected and purchased:

- A modulator (see Chapter 4).
- A signal generator to modulate the diode laser and the modulator. This generator presents high frequency attainable in square wave, two output channels with possibility of frequency matching and delay adjustment.

The signal generator has a limit of 5 V on its output voltage. As the modulator can be driven to up to 15 volts, this puts a limitation on the achievable contrasts.

7.2 Distances computation

To compute the result of the experiments, a program was written using MATLAB[®]. Images are captured and the values of the amplitude, offset and phase-shift are computed with equations (5.2), (5.3) and (5.4).

¹The detailed specifications of the different elements are to be found in Appendix A.

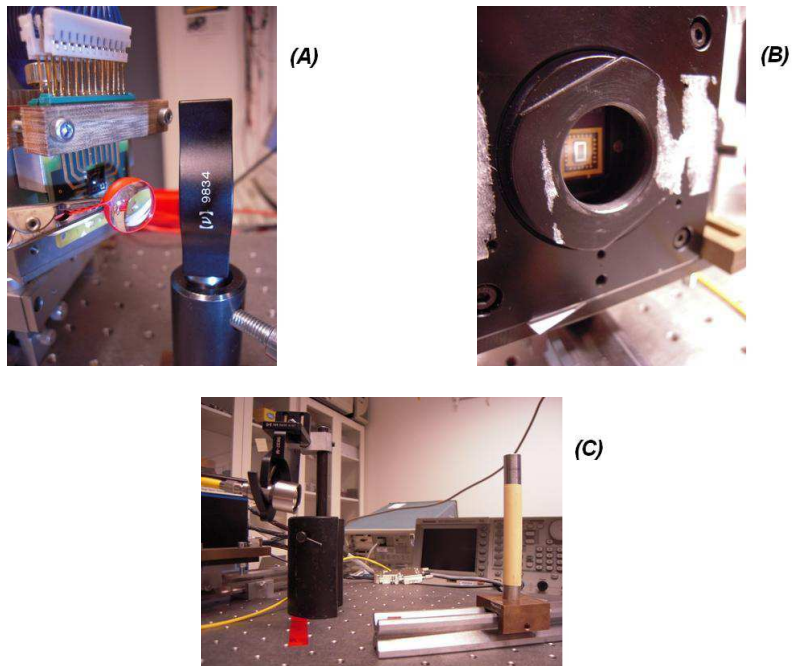


Figure 7.1: Pictures of the experimental setup. (A) shows the modulator and the imaging optics; (B) is the DALSA camera with the CCD sensor; (C) gives an example of illumination of an object.

A region of $m \times m$ pixels is averaged to enhance the signal-to-noise ratio, and the distance is calculated using equation 5.5. The results are displayed in a 3D graph with a Z-scale indicating the depth value.

For each object, a region of interest (ROI) is delimited manually and entered in the program. The second output of the computation is the value of the distance average on the ROI.

The MATLAB[®] source code can be found in Appendix B.

Chapter 8

Experiments

8.1 Preliminary checks

The modulator has a good modulation depth at one specific wavelength. The diode laser is tuned to match this wavelength, and the output power is checked. For modulator B1-1000-L at angle $\theta = 22.5^\circ$, the wavelength must be set at 846 nm. The output power is maximized with 10 mW.

The modulated light profile is also checked. The laser and the modulator are in the experiments driven by square signals. The diode laser appears to follow a square signal at frequencies of tens of MHz. Figure 8.1 shows the laser output for $f_{mod} = 15$ MHz.

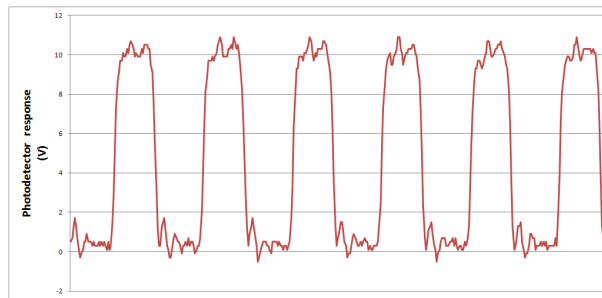


Figure 8.1: Laser output signal for a square wave modulation at $f_{mod} = 15$ MHz.

A test is also run for checking experimentally the response of the modulator to the driving signal. The intensity for different delays between the light source modulation signal and the shutter modulation signal must vary for the results to be valid. The tests show a good contrast for modulation frequencies up to 15 MHz. For frequencies above this value, the images lose a lot of contrast. This confirms what the theory predicts and sets the driving frequency to 15 MHz. At this frequency, the experimental contrast ratio is about 3:1.

8.2 Distance measurements

8.2.1 Parameters

After the preliminary checks, some parameters are chosen and adjustments made:

- The modulation frequency is entered in the signal generator (here, 15 MHz).
- The angle of the modulator is optimized by maximizing the contrast at low frequencies.
- All the background lights are switched off to avoid "contamination" by ambient light.
- The beam divergence is adapted to the range of the measurements by the use of collimators and diffusive filters.
- The initial value of the delay between the two modulation signals is chosen in order to avoid very disruptive non-linear effects.

This last parameter is to be determined experimentally because of electronic and some optical delays difficult to estimate theoretically. A first series of pictures is taken of an object at a distance $D = 60$ cm. For each picture, the initial phase difference between the light modulation signal and the shutter signal is shifted by 10° . Increasing the angle by 10° is equivalent to virtually increasing the distance of the object by 28 cm. The calculations are carried out and averaged on several series of pictures in order to reduce the noises, and the results of the measurements are compared to the expected values. The results are shown in figure 8.2. In order to carry out the measurements in a zone of linearity, the initial phase difference is chosen to be $A_0 = 110^\circ$ for short distances (20-60 cm) or 90° for long distances (60-160 cm).

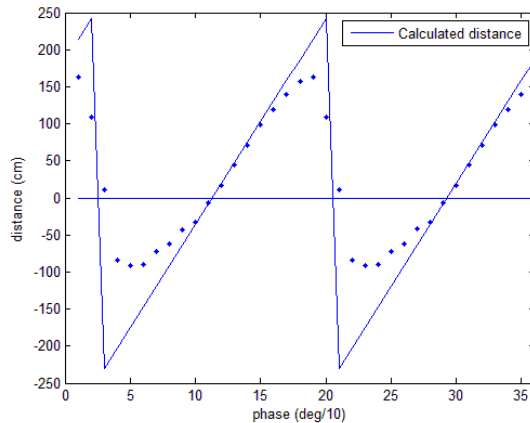


Figure 8.2: Study of non-linearity effects. Comparison between expected distances and averaged value of measured distances.

8.2.2 Image acquisition

An experiment is carried out as follows. An object is placed in the field-of-view of the camera, the light source and the shutter are modulated. The time integration of the CCD sensor is set so that the intensity received on the sensor is sufficient but does not cause saturation. Four pictures of the scene are needed with, in between two pictures taken, a change of 90° in the driving signals' phase difference. The pictures are to be later processed to calculate the distance of the object from the camera. The process is illustrated on figure 9.1.

It is important to notice here that the computation as such cannot give the true distance. Indeed, in the system itself, as delays are introduced, all the distances calculated will be added a certain value compared to the real distance. This value being a constant, it is easy though to evaluate it and calibrate the camera to calculate the real distance values.

To evaluate the offset and test the system, the object was moved along a scale every 10 cm, from 20 cm to 160 cm away. Figure 8.3 shows a picture of the scale. The first measurements, going from 20 cm to 80 cm, were taken using a collimator and a diffusive filter just after the light source, and an initial phase shift $A_0 = 110^\circ$. For measurements at longer distances, the filter was removed to increase the intensity of the illumination, too weak with the filter. The initial phase shift was also changed to $A_0 = 90^\circ$ to ensure that the measurements stay in the linearity zone. The consequence of the changes between short and long range is a change in the offset, that will need to be calibrated twice.

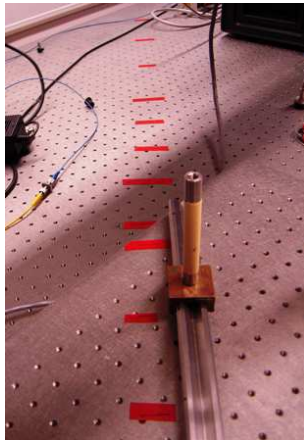


Figure 8.3: Picture of the measurement scale with an object. The scale is made of a graduation every 10 cm, located 20 cm to 160 cm away from the camera.

8.2.3 Problems encountered and solutions found

The main problem encountered when carrying out the images acquisition was the lack of power from the diode laser. As a consequence, the object needed to be close and the camera set with long integration time in order to get enough

light back to the sensor. But with long integration times, the background illumination and possibly some detector noises become an issue, even in an almost totally dark room. For that reason, the measurements could not be done with a wide illumination of the scene further than 80 cm away. A way to get around the problem was to focus the light on the object, so that as much of the available optical power as possible is actually used for the acquisition. This way, it was possible to carry out measurements farther, up to 160 cm (end of the measurement table).

The use of coherent light also leads to a speckle effect that makes the images studded with black and white spots. On close objects this effect is particularly visible. It changes the intensity received for each pixel by a multiplicative factor. In effects, it does not change the value of the distance measured for still objects, but it can affect the resolution. It also alters the quality of the 2D pictures. Moreover, the light beam showed other inhomogeneities not due to the speckle effect. The origin of this noise is unclear, but it showed to be also of multiplicative nature and should not be a problem for the distance calculations, except for the resolution. This was attenuated by tape diffusers when possible.



Figure 8.4: Example of picture taken with the 3D time-of-flight camera. Here, a role of tape Scotch[®]

8.2.4 Limitations

Some issues of the setup itself constitute limitations for the system.

The signal generator presents all the functions needed but is limited in voltage output to 5 volts. A full use of the modulator possibilities would require higher driving voltages. This can be done by electronic means¹.

The field-of-view is quite narrow. Because the modulator is small and the image of the scene focussed with a classical lens, the resulting field-of-view is only 2.3°. Together with the weakness of the illumination light, it makes it impossible to image a wide scene with several objects.

¹This has been tried with a voltage amplifier. It was not implemented on the setup though, because the amplified signal was going to negative voltages, which would damage the modulator.

The system also presents other sources of noise whose effects are difficult to separately visualize. Their global impact on the system's resolution is analysed in the next chapter.

Chapter 9

Results and discussion

The images acquired are loaded manually in the program. The computation results in a 3D image indicating the distance pixel by pixel on a color Z-scale, and the value of the object distance averaged on a region of interest, also defined manually. Figure 9.1 summarizes the complete data acquisition and computation chain.

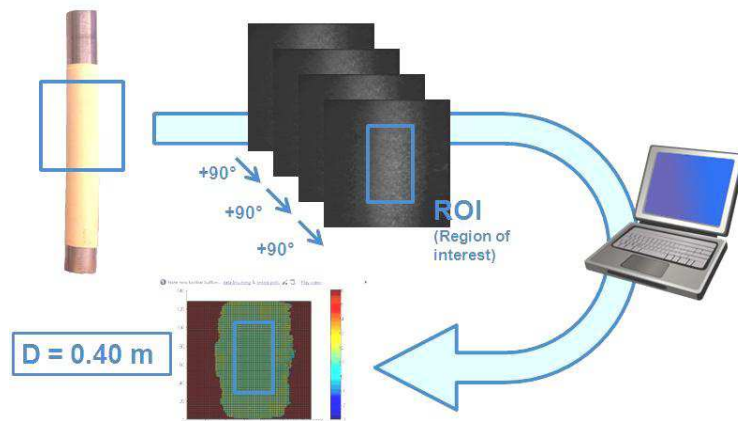


Figure 9.1: Data acquisition and computation.

9.1 Measurements results

The data acquisition and computation process was repeated all along the scale for close and less close objects. As explained in the previous chapter, the system was slightly modified for long distances, leading to two sets of data with a different offset. Graph 9.2 represents the results of the short range measurements, and graph 9.3 shows the long range measurements. Finally, the curves are calibrated and joined together in graph 9.4.

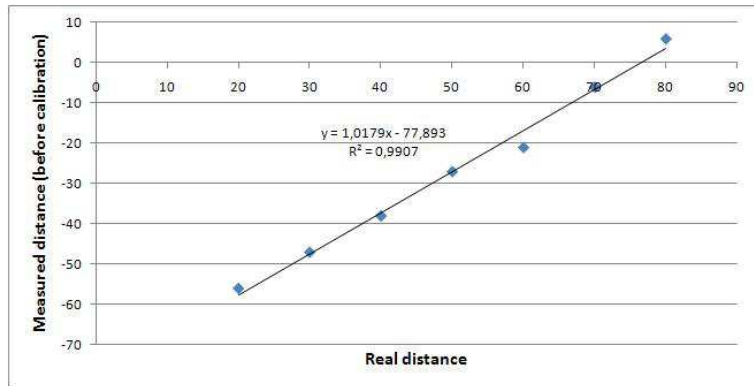


Figure 9.2: Short range measurements.

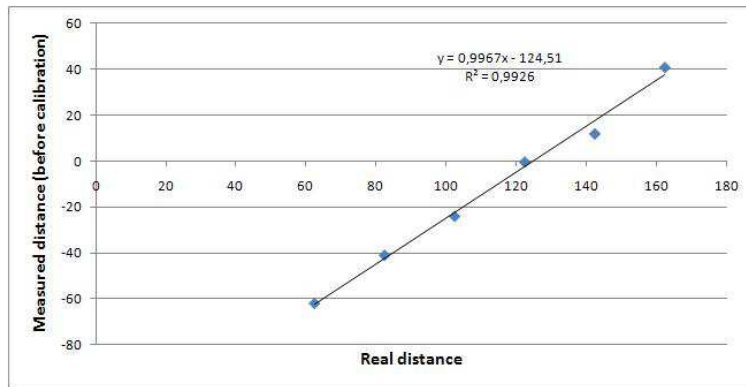


Figure 9.3: Long range measurements.

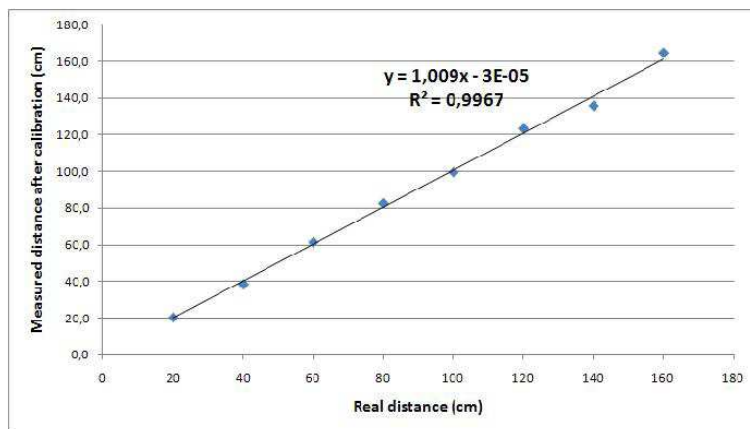


Figure 9.4: Calibrated measurements.

9.2 Evaluation of performances

The measurements gave results close to the real distance values expected after calibration. The maximum difference between real and measured values is 5.5 cm and the standard deviation is 2.9 cm. A further analysis is conducted to define what is the role played by the accuracy and the repetability in the global resolution of the system.

9.2.1 Repetability

The repetability of the system (also called precision) is affected by digitization and noises of all kinds. Most of the noises can be reduced by different devices or techniques. Here, no hardware has been used against noises. The results of the calculations pixel-by-pixel without any further computation are thus giving quite different values. The median filter implemented solves part of the problem by homogenizing the value of each pixel with the values of its $m \times m$ closest neighbours. This way, the pixels with abnormal values do not distort the 3D graph. Then, spatial avering is done on a region of interest (ROI) in order to get an averaged value of the distance on a square of pixels with good intensity.

The repetability of the measurement was determined by computing the results of a same measurement twenty times. The standard deviation on the result is $\sigma = 0.8$ cm. an example of statistical distribution is shown in figure 9.5.

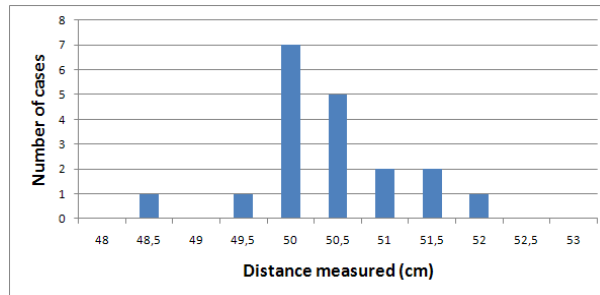


Figure 9.5: Repetability estimation: example of statistical distribution of measured distance value for 20 measurements at distance $D = 50$ cm.

The impact of the definition of the ROI and the choice of median filter on the results is also evaluated. For several sets of images, distance computations have been made while varying the position and size of the ROI. The standard deviation of the data set is $\sigma' = 1.4$ cm. The choice of value for the median filter also has an impact on the averaged value. For $m = 3$ to $m = 7$, the standard deviation on the result is $\sigma'' = 0.9$ cm.

The final standard deviation, taking into account the different parameters, is $\sigma_{tot} = 1.8$ cm (mean squared error). The margin of error is typically about twice the standard deviation (radius of a 95% confidence interval) [20]. The

repeatability of the system is thus evaluated to 3.6 cm.

9.2.2 Accuracy

The results can also present a systematic error, defined as the accuracy of the system. The linearity test presented in graph 8.2 showed that, from a phase difference between the two signals of 100° to 140° , corresponding to a distance range of 20 cm to 160 cm, the measured values were fitting quite well the theoretical values. Nevertheless, there is a systematic error on this range that is more important for the extreme distance values, giving an accuracy on this range of 3.3 cm.

9.2.3 Global resolution

The system, on the range of measurements taken, has a global resolution evaluated to $3.6 \text{ cm} + 3.3 \text{ cm} = 6.9 \text{ cm}$ at worst (at the extremities of the measurement scale). It is important to keep in mind that this value is valid on a 20-160 cm range. It cannot be generalized to the entire 10 m of possible measurement range because of the non-linearity issue. The resolution also depends on the intensity received on the sensor. For objects with lower reflectivity in the near-infrared, the resolution can get worse.

However, this value does not represent the final resolution of the system. The precision can be improved by temporal averaging, and the error due to the accuracy can be compensated by post-processing or reduced by some improvement of the measurement technique.

9.3 Limitations and solutions: summary

Limitation	Cause(s)	Solution(s)
Low illumination	Laser output power	New laser; optical amplifier
Maximum driving frequency	Modulator size	Array of small modulators
Modulation depth	Signal generator max. output voltage	Electronic amplifier; bias-tee
High offset	Background lighting	Optical filter
	Detector noises	Cooling; exposure time reduction
Systematic errors	High-orders harmonics	Sine-wave modulation; heterodyne method; harmonic rejection technique; post-processing
Digitization error	8-bit coding	12-bit coding
Illumination noise	Speckle effect	Diffuser; post-processing
	Beam inhomogeneities	
Narrow field-of-view	Modulator size	Array of small modulators
Limit on optical power	Eye-safety	Change to $\lambda = 1.5 \mu\text{m}$

Chapter 10

Conclusion and perspectives

The aim of the project was to design, build and evaluate the performances of 3D time-of-flight camera. The challenge, which was to get a working demonstrator made of simple and low-cost components, was successfully handled.

The key component of the demonstrator is the surface-normal multiple quantum well electro-absorption modulator. Intended to be used as fast optoelectronic shutter, this modulator is the innovation of this 3D time-of-flight system. Consequently, time was spent to characterize its properties. First, its maximum modulation frequency is inversely proportional to its area, meaning that a trade-off between modulation frequency and modulator size is to be made. Second, the absorption spectrum of this modulator was characterized to determine the optimum working wavelength and the contrast ratio for different illumination angles.

The focus was also brought on the different existing methods for signal computation and distance measurement. The two main methods for continuous wave modulation were studied with their advantages and drawbacks. The homodyne method was chosen for its simpler implementation and a MATLAB[®] program was written to compute the data.

The demonstrator was designed and assembled taking into account the choice of modulator, illumination angle and signal analysis method. Eventually, the evaluation of the performances showed, with a classical homodyne method at modulation frequency $f_{mod} = 15$ MHz and illumination angle of 22.5° , an accuracy of 3.3 cm in the worst case and a repeatability of 3.6 cm on a measurement range of 1.5 m. This last value can be improved by temporal averaging at the expense of reduced frame rate.

Such a system does not present the same performances as the time-of-flight cameras already commercialized (see Chapter 2 for comparison). It can nevertheless be improved, and presents a good alternative in terms of prices.

The type of modulator used for this project can achieve really high contrast ratios, although the present configuration it is limited to about 3:1. From the experimental results, two conclusions can be drawn concerning the use of the

modulator:

1. Placing the modulator in normal reflection, or modifying its layers' structure to match an optimum contrast ratio in non-normal reflection, could enhance the performances.
2. Other types of modulators with optimum contrast ratios of 4:1 can also be used as shutters. In particular, one InP modulator has been developed that exhibits such contrast ratios around $1.5 \mu\text{m}$. This wavelength is eye-safe and consequently more powerful illumination can be sent than with the present modulator.

The low optical power from the diode laser played a big role in the choices made during this project. In order to extend the camera range and investigate further the possibilities of the designed system, it is strongly recommended to increase the illumination power to several tens or hundreds of milliwatts. This improvement would also permit other changes:

- The field-of-view could be widened to larger illuminated scenes. This possibility also requires though a change in the system, either in the optics or in the modulator itself. More advanced optics could increase the field-of-view or, more conveniently, to use an array of modulators rather than a single one. The second solution would enable the user to keep a high modulation frequency while increasing the modulator size. The size of individual modulators could also be reduced to match higher frequencies. Nevertheless, it also presents new challenges: 1. it is tricky to drive several modulators together and 2. a bigger area could cause aberrations on the edges in non-normal reflection on the surface, although this disadvantage can probably be solved by post-processing.
- The normal reflection configuration can be tested to use the full potential of the modulator.

Another recommended improvement is to try to modulate with other wave forms, or to implement the heterodyne method, known for giving more accurate results on the distance measurements. Instead of a signal generator, one might also prefer to program a Field-programmable Gate Array (FPGA) in order to have more liberties on the modulation (for example, to apply the harmonic rejection sampling method proposed by A.D.Payne *et al* [13]). However, the heterodyne method is more difficult to implement and could be demanding in terms of computation time and costs.

Acknowledgements

First of all, I would like to thank my supervisor at Acreo, Bertrand Noharet, for entrusting me with this project. It has been a very interesting experience to work for this research institute, halfway between industries and universities. During five months this project was going on, Bertrand has been there to advise me, help me when things were getting tricky, and encourage me. He shared with me his experience on many technical and not-so-technical subjects, and working under his supervision has been a real pleasure.

I am also deeply grateful to Stéphane Junique, who has always been there to help me and answer my never-ending questions, as well as to have a friendly chat between two experiments. My special thanks also go to Qin Wang, who gave me a very helpful hand with the modulators and my work in general; to Susan Almqvist, who took on her time to wire-bond the modulators for my project; to Leif Kjellberg, who contributed to the realization of the experimental setup by helping with the driving electronics; to Teresita Qvanström, for taking care of my 'Swedish education'.

I would also like to thank all the people at Acreo for making this few months such a nice time, especially to all the fellow students I shared the office with: Ali (Pooryah) Asadollahi, Boban (Quantum Rods Farmer) Gavric, Ludwig (Lud') Östlund and Norbert Kwietniewski. Thank you also to the 'second more crowded room' occupiers, Romain Esteve, Jang-Kwon Lim and Sergey Reshanov, for the enjoyable moments at lunch and coffee breaks.

This project would never have been possible without the financial fundings from the IMAGIC center and its investors. I am grateful to all the people who believed in this project and chose to support it.

And last, but not least, I would like to thank my parents Jean and Cécile van Frank, as well as my dear friends Emilie Merlen and Florian Toth, who, despite the distance, always gave me all their love and support.

Bibliography

- [1] Adapted from http://en.wikipedia.org/wiki/Time-of-flight_camera
- [2] R. Lange, P. Seitz, "Seeing distances – a fast time-of-flight 3D camera", *Sensor Review, Vol. 20 Iss: 3, pp.212–217* (2000)
- [3] T. Ringbeck, "A 3D time of flight camera for object detection", *Sensor Review, Vol. 20 Iss: 3, pp.212–217* (2000), retrieved from <http://www.ifm-electronic.kr/obj/01D.Paper-PMD.pdf>.
- [4] R. Kaufmann, M. Lehmann, M. Schweizer, M. Richter, P. Metzler, G. Lang, T. Oggier, N. Blanc, P. Seitz, G. Gruener and U. Zbinden, "A time-of-flight line sensor: development and application", *Proc. SPIE 5459, 192* (2004); doi:10.1117/12.545571
- [5] S. B. Gokturk, H. Yalcin, C. Bamji, "A Time-Of-Flight Depth Sensor – System Description, Issues and Solutions", *Proceedings of the 2004 Conference on Computer Vision and Pattern Recognition Workshop (CVPRW'04) Volume 3 - Volume 03 (CVPRW '04), Vol. 3. IEEE Computer Society, Washington, DC, USA, 35-* (2004)
- [6] Adapted from <http://www.hizook.com/blog/2010/03/28/low-cost-depth-cameras-aka-ranging-cameras-or-rgb-d-cameras-emerge-2010>
- [7] Adapted from http://www.pmdtec.com/fileadmin/pmdtec/downloads/documentation/datasheet_o3_v0100.pdf
- [8] Adapted from http://www.mesa-imaging.ch/dlm.php?fname=pdf/SR4000_Data_Sheet.pdf
- [9] Adapted from http://www.fotonic.com/assets/documents/fotonic_b40.pdf
- [10] S. Junique [thesis], "Surface-normal multiple quantum well electroabsorption modulators : for optical signal processing and asymmetric free-space communication", *Stockholm: KTH. Trita-ICT/MAP, 2007:8.* (2007)
- [11] A. A. Dorrington, D. A. Carnegie, M. J. Cree, "Toward 1-mm depth precision with a solid state full-field range imaging system", *Proc. SPIE 6068, 60680K* (2006); doi:10.1117/12.641980

- [12] R. M. Conroy, A. A. Dorrington, R. Knemeyer, M. J. Cree, "Range imager performance comparison in homodyne and heterodyne operating modes", *Proc. SPIE 7239, 723905* (2009); doi:10.1117/12.806139
- [13] A. D. Payne, A. A. Dorrington, M. J. Cree, D. A. Carnegie, "Improved linearity using harmonic error rejection in a full-field range imaging system", *Proc. SPIE 6805, 68050D* (2008); doi:10.1117/12.765930
- [14] A. A. Dorrington *et al.*, "Achieving sub-millimetre precision with a solid-state full-field heterodyning range imaging camera", *Meas. Sci. Technol. 18 2809* (2007); doi: 10.1088/0957-0233/18/9/010
- [15] Adapted from <http://www.canesta.com/assets/pdf/technicalpapers/Canesta101.pdf>
- [16] C. Baud, H. Tap-Bteille, M. Lescure, J.-P. Bteille, "Analog and digital implementation of an accurate phasemeter for laser range finding", *Sensors and Actuators A: Physical, Volume 132, Issue 1, Pages 258-264* (2006); doi:10.1016/j.sna.2006.06.005
- [17] D. A. Carnegie, M. J. Cree, A. A. Dorrington, "A high-resolution full-field range imaging system", *Rev. Sci. Instrum. 76, 083702* (2005); doi:10.1063/1.1988312
- [18] B. L. Stann, M. M. Giza, D. Robinson, W. C. Ruff, S. D. Sarama, D. R. Simon, Z. G. Sztankay, "Scannerless imaging ladar using a laser diode illuminator and FM/cw radar principles", *Proc. SPIE 3707, 421* (1999); doi:10.1117/12.351363
- [19] R. Lange [thesis], "3D Time-of-Flight Distance Measurement with Custom Solid-State Image Sensors in CMOS/CCD-Technology", *Department of electrical engineering and computer science, University of Siegen* (2000)
- [20] Adapted from http://en.wikipedia.org/wiki/Standard_deviation

Appendix A

List of material specifications

Camera

- DALSA CA-D1-0128A-STDN
- 128x128 pixels
- 16 μm square pixels with 100% fill factor
- 8-bit digital, dynamic range 256:1
- 16 MHz max
- Noise Equivalent Exposure: 36 pJ/cm²
- Saturation Equivalent Exposure: 23 nJ/cm²

Laser

- Toptica Photonics DL100
- FIDL-150S-850C
- Tunable range: 810 nm - 865 nm
- Maximum input current: 73 mA
- Achievable output power: 10 mW

Function generator

- Tektronix AFG3252
- 2 output channels
- Arbitrary waveforms
- Frequency 1 mHz to 240 MHz
- Independant or synchronized settings on channels

Super-Luminescent Diode

- Superlum SLD-381-MP2-DIL-SM-PD
- Range 820 nm - 865 nm
- pigtailed

Optical Spectrum Analyser

- StellarNet EPP2000 HR UVN-SR
- Range: 200 nm - 1100 nm

Photodiode

- Thorlabs PDA10A-EC
- Si-amplified detector
- Range: 200 nm - 1100 nm
- Bandwidth: 150 MHz
- Gain: 1×10^4 V/A
- Maximum responsivity: 0.45 A/W

Appendix B

Program for distance computation

```
%%%%%%%%%%%%%%%%%%%%%%%%%%%%%%%%%%%%%%%%%%%%%%%%%%%%%%%%%%%%%%%%%%%%%%%%
%%%      ExtractData      %%%
%%%%%%%%%%%%%%%%%%%%%%%%%%%%%%%%%%%%%%%%%%%%%%%%%%%%%%%%%%%%%%%%%%%%%%%%

%%% MATLAB program to compute results from homodyne detection.
% 4-buckets method.

clear all;
% Number of pixels in a line/row
N=128;
% Driving frequency:
f = 15E6; % INPUT
% Speed of light
c = 2.99E8;
% Median filter
m = 3;
% Background illumination
BG = 20; % INPUT

% Region of interest
% Horizontally
Hmin = 55; % INPUT
Hmax = 75; % INPUT
% Vertically
Vmin = 55; % INPUT
Vmax = 75; % INPUT

% Initialization
Amplitude=zeros(N,N);
Offset=zeros(N,N);
```

```

PhaseShift=zeros(N,N);
Distance=zeros(N,N);
Av = 0;
AvA = 0;
Av0 = 0;

%%% IMAGES % INPUTS
Pic1=imread('C:\...\90\3D_image00000.png','png');
Pic1=rgb2gray(Pic1);
Pic2=imread('C:\...\180\3D_image00000.png','png');
Pic2=rgb2gray(Pic2);
Pic3=imread('C:\...\-90\3D_image00000.png','png');
Pic3=rgb2gray(Pic3);
Pic4=imread('C:\...\0\3D_image00000.png','png');
Pic4=rgb2gray(Pic4);

%%% Calculation Amplitude, Phase, Offset and Distance
for i=1:N
    for j=1:N
        temp1=double(Pic1(i,j)-BG);
        temp2=double(Pic2(i,j)-BG);
        temp3=double(Pic3(i,j)-BG);
        temp4=double(Pic4(i,j)-BG);
        temp5=(temp1-temp3)^2;
        temp6=(temp2-temp4)^2;

        Amplitude(i,j) = ((temp5+temp6)^0.5)/2;

        if (abs(temp2-temp4)>2)
            PhaseShift(i,j) = atan((temp1-temp3)/(temp2-temp4));
        else PhaseShift(i,j)= 2*pi;
        end;

        Offset(i,j) = (temp1+temp2+temp3+temp4)/4;
        Distance(i,j) = PhaseShift(i,j)*c/(4*pi*f) ;
    % d=phase*c/(4*pi*freq)
    end;
end;

%%% Filter application
Distance = medfilt2(Distance, [m m]);

%%% Calculation average distance on ROI
for i=Hmin:Hmax
    for j=Vmin:Vmax
        Av = Av + Distance(j,i);
        AvA = AvA + Amplitude(j,i);
        Av0 = Av0 + Offset(j,i);
    end;
end;

```

```

% Distance, amplitude and offset averaged on the ROI
Av = Av / ( (Hmax-Hmin+1)*(Vmax-Vmin+1) )
AvA = AvA / ( (Hmax-Hmin+1)*(Vmax-Vmin+1) )
AvO = AvO / ( (Hmax-Hmin+1)*(Vmax-Vmin+1) )

%%% GRAPHS
% Note: Upside down compared to initial image because of
% the origin that is placed on the bottom left corner.

%%% Display distance
figure;
[x,y]=meshgrid(0:1:128,0:1:128);
surf(Distance);
colormap;
caxis([-3 6]);

%%% Display amplitude
figure;
[x,y]=meshgrid(0:1:128,0:1:128);
surf(Amplitude);
colormap;

%%% Display offset
figure;
[x,y]=meshgrid(0:1:128,0:1:128);
surf(Offset);
colormap;

```